Soft Matter

Molecular Interactions of Phospholipid Monolayers with a Model Phospholipase

Journal:	*Soft Matter*
Manuscript ID	SM-ART-06-2018-001154.R3
Article Type:	Paper
Date Submitted by the Author:	30-Mar-2019
Complete List of Authors:	Zhang, Pin; University of Illinois at Chicago, Chemical Engineering Villanueva, Veronica; University of Illinois at Chicago, Chemical Engineering Kalkowski, Joseph; University of Illinois at Chicago , Chemical Engineering Liu, Chang; University of Illinois at Chicago, Chemical Engineering Donovan, Alexander; University of Illinois at Chicago, Chemical Engineering Bu, Wei; University of Chicago, Center for Advanced Radiation Sources Schlossman, Mark; University at Illinois at Chicago, Department of Physics Lin, Binhua; University of Chicago, James Franck Institute and CARS Liu, Ying; University of Illinois, Chemical Engineering

Soft Matter

ARTICLE

Molecular Interactions of Phospholipid Monolayers with a Model Phospholipase

Received 00th January 20xx,
Accepted 00th January 20xx

DOI: 10.1039/x0xx00000x

www.rsc.org/

Pin Zhang, [a] Veronica Villanueva, [a] Joseph Kalkowski, [a] Chang Liu, [a] Alexander Donovan, [a] Wei Bu, [b] Mark L. Schlossman, [c] Binhua Lin, [b] and Ying Liu [a]*

The intrinsic overexpression of secretory phospholipase A2 ($sPLA_2$) in various pro-inflammatory diseases and cancers has the potential to be exploited as a therapeutic strategy for diagnostics and treatment. To explore this potential and advance our knowledge of the role of $sPLA_2$ in related diseases, it is necessary to systematically investigate the molecular interaction of the enzyme with lipids. By employing a Langmuir trough integrated with X-ray reflectivity and grazing incidence X-ray diffraction techniques, this study examined the molecular packing structure of 1,2-palmitoyl-sn-glycero-3-phosphocholine (DPPC) films before and after enzyme adsorption and enzyme-catalyzed degradation. Molecular interaction of $sPLA_2$ (from bee venom) with the DPPC monolayer exhibited Ca^{2+} dependence. DPPC molecules at the interface without Ca^{2+} retained a monolayer organization; upon adsorption of $sPLA_2$ to the monolayer the packing became tighter. In contrast, $sPLA_2$-catalyzed degradation of DPPC occured in the presence of Ca^{2+}, leading to disruption of the ordered monolayer structure of DPPC. The interfacial film became a mixture of highly ordered multilayer domains of palmitic acid (PA) and loosely packed monolayer phase of 1-palmitoyl-2-hydroxy-sn-glycero-3-phosphocholine (lysoPC) that potentially contained the remaining un-degraded DPPC. The redistribution of lipid degradation products into the third dimension, which produced multilayer PA domains, damaged the structural integrity of the original lipid layer and may explain the bursting of liposomes observed in other studies after a latency period of mixing liposomes with $sPLA_2$. A quantitative understanding of the lipid packing and lipid-enzyme interaction provides an intuitive means of designing and optimizing lipid-related drug delivery systems.

Introduction

Optimizing the design of drug delivery vesicles for specific targeting of drug compounds to disease cells and tissues can maximize drug efficacy while minimizing unwanted side-effects. Lipid nanovesicles, because of their similar composition to cell membranes, have been applied as one of the prominent nanomedicine platforms approved by the U.S. Food and Drug Administration (FDA).[1] However, lipid vesicles for drug delivery suffer from low stability upon blood dilution and insufficient drug release at the target site. As one promising method of increasing local drug release from lipid vesicles, overexpressed intrinsic enzymes such as secretory phospholipase A2 ($sPLA_2$) have been used to trigger vesicle structural change.[2] Previous studies have demonstrated that $sPLA_2$ is overexpressed in a variety of inflammatory metabolic diseases[3, 4] including cancers, and the enzyme level is strongly related to cancer stage[5] and tumor metastasis.[6] As a lipolytic enzyme, $sPLA_2$ can catalyze the hydrolysis of one tail of a phospholipid, which yields equimolar fatty acid and lysophospholipid. This catalytic activity relies on phospholipid composition and packing, substrate morphology, as well as environmental conditions.[7] Most $sPLA_2$ isoforms require Ca^{2+} to be active, and their active sites generally contain His-Asp motifs.[8, 9] The numerous possible combinations of parameters have made it difficult to design drug-delivery lipid vesicles through empirical trials. Therefore, it is essential to achieve a fundamental understanding of molecular interactions of phospholipids with enzymes.

Morphological transformations of lipid films upon $sPLA_2$ adsorption and catalyzed degradation have been studied using many techniques, such as fluorescence microscopy,[10, 11] atomic force microscopy,[12, 13] polarization-modulated Fourier transform infrared spectroscopy,[14] and grazing incidence X-ray diffraction.[15] Studies have shown that the degradation begins at interfacial defects and liquid-gel phase boundaries. As the degradation proceeds, the substrates and degradation products may re-organize the molecular packing of the film and generate new domains where fluorescence-labeled $sPLA_2$ can accumulate.[11, 16-18] Reichert et al. discovered that the new domains were rich in fatty acids.[11] Maloney and Grainger observed that these new domains occurred only on alkaline subphase containing Ca^{2+} ions.[18] Grandbois et al. reported a formation of calcium-palmitate complexes at the interface after the degradation of 1,2-palmitoyl-sn-glycero-3-phosphocholine (DPPC) films.[14] A recent study by Hong has found that new domains might have three-dimensional crystal-like structures that induce non-specific lipoprotein binding, providing one possible explanation for

[a] Department of Chemical Engineering, University of Illinois at Chicago, Chicago, IL 60607.
[b] Center for Advanced Radiation Sources, University of Chicago, Chicago, IL 60637.
[c] Department of Physics, University of Illinois at Chicago, Chicago, IL 60607.
* liuying@uic.edu
† Electronic Supplementary Information (ESI) available: [details of any supplementary information available should be included here]. See DOI: 10.1039/x0xx00000x

the contribution of $sPLA_2$ to the development of vascular diseases.[19] In addition, the molecular re-organization may contribute to the degradation kinetics of the substrates.[20, 21] Therefore, investigation of the detailed interfacial organization of the lipid substrate and degradation products will provide a better understanding of the roles of $sPLA_2$ in related physiological processes and help to design and optimize lipid-based drug delivery systems.

The two products generated from phospholipid degradation, fatty acids and lysophospholipids, are known to increase liposome permeability.[22, 23] High concentrations of fatty acids and lysophospholipids may cause cell lysis[22, 24] and metabolic disease.[25] Also, the presence of Ca^{2+} is essential for the process of membrane degradation.[26, 27] Here, we explore the mechanistic effects of degradation products on membrane perturbation and the role of Ca^{2+}.

To gain molecular-level insight into lipid film degradation, a Langmuir trough integrated with synchrotron X-ray interface-sensitive techniques at ChemMatCARS Sector 15C of the Advanced Photon Source (APS) at Argonne National Laboratory was employed.[28-30] The saturated phospholipid DPPC was studied because it is widely used in drug delivery systems and is one of the main components of cell membranes. X-ray reflectivity and grazing incidence X-ray diffraction (GIXD) were used to measure the change in interfacial organization of DPPC monolayers that occurred upon $sPLA_2$ adsorption and catalyzed degradation. Measurements were taken in the presence and absence of Ca^{2+} in the buffer subphase. As a comparison, the molecular packing structures of the individual degradation products of DPPC, palmitic acid (PA) and 1-palmitoyl-2-hydroxy-sn-glycero-3-phosphocholine (lysoPC) and their equimolar mixture (PA-lysoPC) were investigated separately.

Experimental

Materials and Reagents

DPPC and lysoPC were purchased from Avanti Polar Lipids. PA (> 99%), honey bee (*Apis mellifera*) venom $sPLA_2$, calcium chloride dehydrate, and hydrochloric acid were purchased from Sigma-Aldrich. Tris base was purchased from Fisher. The subphase buffer with calcium (Ca buffer) was 5 mM $CaCl_2$ and 8 mM Tris. The subphase buffer without calcium (Ca-free buffer) was 8 mM Tris. The pH of both buffers was adjusted to 7.4 by adding diluted hydrochloric acid (3.7 v%). All buffers were prepared and exposed to vacuum for 3 hours to reduce dissolved oxygen. The change in Ca^{2+} concentration was less than 0.1% after degassing. Organic solvents, including methanol, ethanol, and chloroform, were purchased from Sigma-Aldrich. De-ionized water (18.2 MΩ, MILLIPORE) was used in all experiments. All chemicals were purchased at standard grades and used as received.

X-ray Measurements

A customized Teflon trough (78 x 177.6 mm^2) with a single barrier and a magnetic stirrer (labdisc, Fisherbrand) attached on the bottom was placed within a box integrated within the path of the X-ray beamline, see **Figure s1** in Supplemental Information (**SI**) for a schematic drawing of the setup. Interfacial pressure was measured with a Wilhelmy paper plate hung from an electronic balance. The X-ray wavelength was 1.24 Å. Reflectivity and GIXD data were collected with a Pilatus 100K area detector. The trough was shifted during measurements to probe areas of the film that were previously unexposed to X-rays in order to minimize radiation damage. All experiments were conducted at roughly 22.7 °C.

Lipids were dissolved in chloroform and stored at -20°C. Before each experiment, the trough was cleaned and filled with 65 mL of buffer as the subphase. Trough surface cleanliness was confirmed if variations of surface pressure were less than 0.2 mN/m when the barrier was moved its full extent over the buffer surface. A known amount of lipid solution was spread on the interface in a dropwise manner, immediately after which the box containing the trough was sealed and purged with helium gas. All measurements were conducted under helium (with oxygen less than 2%) to reduce radiation damage. The lipid film was then compressed by the barrier at a rate of 6.4 mm/min (i.e., 4.1 $Å^2$ $molecule^{-1}$ min^{-1} for DPPC) until reaching a target surface pressure, which was kept constant during X-ray reflectivity and GIXD measurements. After the measurements, the barrier position was fixed to maintain a constant area and 32.5 µL of a 2 µg/mL $sPLA_2$ solution was injected under the barrier into the subphase. Gentle stirring for 1 hour ensured homogeneous mixing. The monolayer was then allowed to sit unperturbed for another hour to reach quasi-equilibrium, which we define as a change of surface pressure less than 0.1 mN/m over any 2-minute period.

X-ray Data Analysis

X-ray reflectivity data were normalized by the Fresnel reflectivity R_F of an ideal flat interface whose electron density varies as a step function across the interface. A box-model was employed to fit the normalized reflectivity data. Electron density profiles were described as follows:

$$\rho(z) = \frac{1}{2}\sum_{i=0}^{N+1} \mathrm{erf}\left(\frac{z-z_i}{\sqrt{2}\sigma}\right) * (\rho_{i+1} - \rho_i) + \frac{\rho_0}{2} \quad (1)$$

where *erf* is the error function; N = 2, 3, or 4 is the number of slabs within the interface and N+1 is the number of internal interfaces within the interfacial structure; z_i is the position of the i^{th} slab; σ is the interfacial roughness; ρ_i is the electron density of the i^{th} slab; ρ_0 is the electron density of the subphase. Box model parameters were determined by the Parratt formalism using a nonlinear least-squares fit to the reflectivity data.[31]

Two types of box-models were used in this study. Lipid films with homogenous interfacial organization were analyzed by a single-phase box model. Heterogeneous films with phase-separated domains were analyzed by a multi-phase box model with incoherent addition of reflectivity from different domains,[32]

$$R_{incoherent} = \Sigma\, C_i R_i, \quad (2)$$

where C_i is the fractional interfacial coverage of the i^{th} domain, $\Sigma\, C_i$=1, and R_i is the reflectivity from the i^{th} domain.

GIXD provides information on the lateral molecular organization of the lipid films.[33, 34] Bragg peaks were obtained by integrating intensities over the measured range of vertical momentum transfer Q_z along the direction of horizontal momentum transfer Q_{xy} and were

fitted using Gaussian functions to reveal the two-dimensional lattice structures of lipid molecular packing. Integration of intensities over the Q_{xy} of each Bragg peak along the Q_z direction generated the corresponding Bragg rods. Bragg rods were analyzed with the distorted wave Born approximation (DWBA)[35] to provide information on molecular tilting and thickness of the corresponding lipid layers.

Results and discussion

The section of results and discussion begins with comparison of X-ray reflectivity and GIXD measurements on the DPPC film, DPPC film after $sPLA_2$ adsorption (on the Ca-free buffer), and DPPC film after $sPLA_2$-catalyzed degradation (on the Ca buffer), revealing the apparent molecular packing structural changes of the lipid films (**Section 1**). While $sPLA_2$ adsorption resulted in tighter packing of the phospholipid monolayers at the interface, the degraded DPPC film exhibited complicated multi-layer, multi-phase packing structures, which were further analyzed (**Sections 2** and **3**). Interfacial organization of DPPC degradation products, lysoPC and PA, were individually analysed (**Section 2**). The degraded DPPC film was analysed, considering the combination of monolayer lysoPC domains and multilayer PA domains (**Section 3**). Following the results, more implications of the observed structural reorganization through phospholipid-$sPLA_2$ interactions were discussed (**Section 4**).

1. Interfacial structure change of DPPC films upon adding $sPLA_2$ to Ca and Ca-free buffered subphase.

Figure 1A shows X-ray reflectivity curves of the DPPC monolayer (labeled DPPC), the DPPC monolayer after enzyme adsorption (obtained by adding $sPLA_2$ to the subphase without Ca^{2+}, labeled DPPC-$sPLA_2$), and the film after DPPC degradation (obtained by adding $sPLA_2$ to the subphase with Ca^{2+}, labeled degraded DPPC). The derived electron density profiles of the DPPC monolayer and the DPPC monolayer with enzyme adsorption are presented in the inset to **Figure 1A**. GIXD measurements of the DPPC and DPPC-$sPLA_2$ are

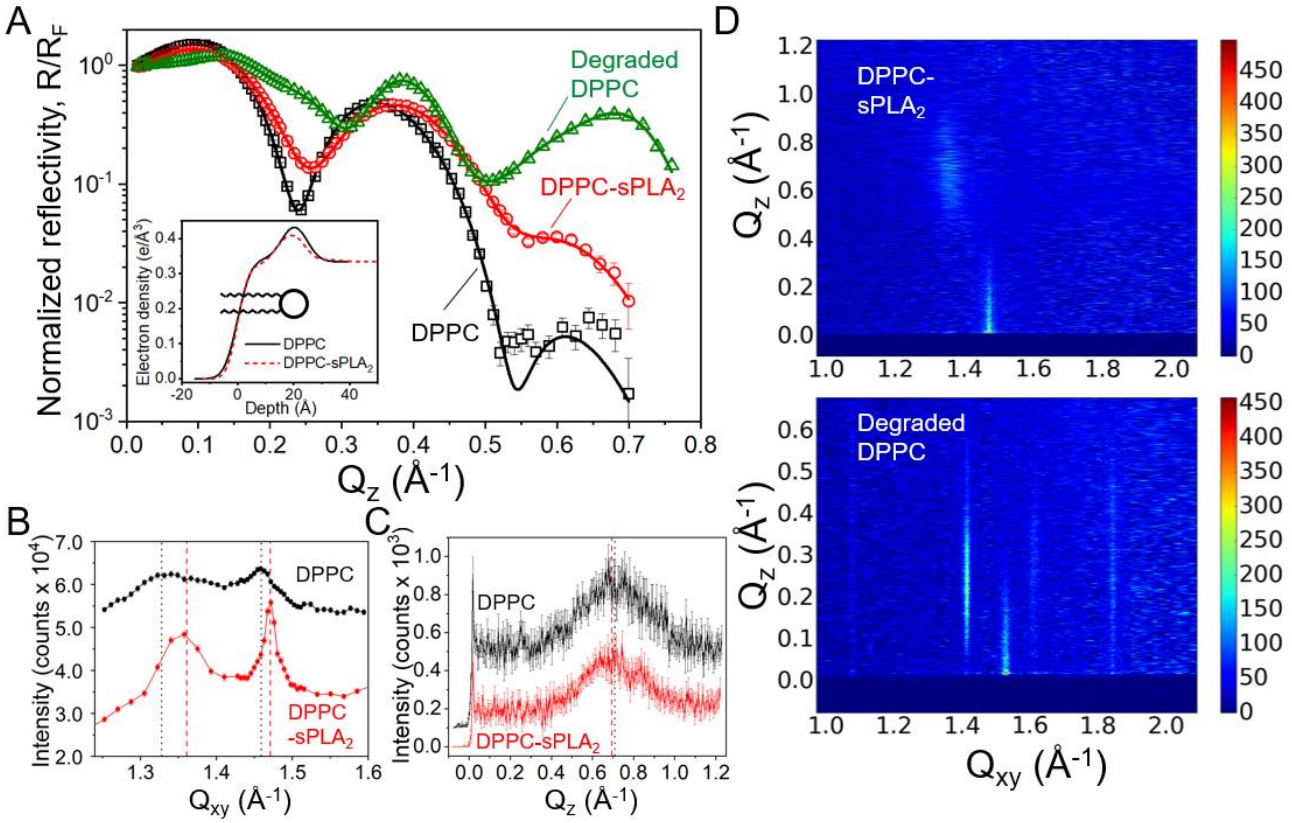

Figure 1. X-ray reflectivity and GIXD results of DPPC film before and after adding $sPLA_2$ to the subphase Ca and Ca-free buffers. (A) Normalized reflectivity of DPPC film (DPPC, black squares) on Ca buffer, DPPC film after $sPLA_2$ adsorption on Ca-free buffer (DPPC-$sPLA_2$, red circles), and DPPC film after degradation on Ca buffer (degraded DPPC, green triangles). The inset displays electron density profiles for the DPPC and DPPC-$sPLA_2$ films. Solid lines show best fits to the data. The structural parameters resulted from model fitting of the X-ray reflectivity data of the DPPC and DPPC-$sPLA_2$ were listed in **Table 1**. The structural parameters from model fitting of the X-ray reflectivity data of the degraded DPPC film were listed in **Table 3**. (B) Bragg peaks and (C) Bragg rods of DPPC and DPPC-$sPLA_2$ films. The data are offset for clarity. The vertical black dotted lines and red dashed lines respectively represent the peak positions for DPPC and DPPC-$sPLA_2$ films. Every three points of each Bragg rod data were grouped together for clarity. (D) Two-dimensional GIXD results for DPPC-$sPLA_2$ (top) and degraded DPPC (bottom) films.

Table 1. Structural parameters resulted from model fitting of X-ray reflectivity data of DPPC and DPPC-sPLA$_2$ (corresponding to the red and black curves in **Figure 1A**). The first slab (labelled 1) is in contact with the aqueous subphase, and the last slab is in contact with vapor.

Parameter	DPPC	DPPC-sPLA$_2$
σ (Å)	$3.8^{+0.1}_{-0.1}$	$3.1^{+0.1}_{-0.3}$
d_1(Å)	$8.0^{+0.8}_{-0.5}$	$13.1^{+0.5}_{-1.6}$
ρ_1 (e/Å^3)	$0.470^{+0.007}_{-0.009}$	$0.340^{+0.001}_{-0.001}$
d_2 (Å)	$16.3^{+0.3}_{-0.6}$	$7.2^{+0.8}_{-4.4}$
ρ_2 (e/Å^3)	$0.340_{-0.003}$	$0.422^{+0.069}_{-0.004}$
d_3 (Å)		$4.0^{+4.0}_{-1.2}$
ρ_3 (e/Å^3)		$0.390^{+0.024}_{-0.019}$
d_4 (Å)		$12.6^{+1.0}_{-1.2}$
ρ_4 (e/Å^3)		$0.324^{+0.004}_{-0.003}$
χ^2	5.4	4.0

The electron density of the aqueous phase was 0.334 e/Å^3 for both Ca and Ca-free buffers. The error bar for each parameter was calculated based on one standard deviation from the best fit value. The electron density of alkyl chain tail was constrained to the range 0-0.34 e/Å^3, the thickness of single head group layer in DPPC-sPLA$_2$ film was constrained to the range 0-8 Å.

Table 2. Structural parameters resulted from model fitting of X-ray reflectivity data of lysoPC and PA films on Ca buffer, (corresponding to **Figure 2A**). For PA film, a two-phase box model was used. The first slab (labelled 1) is in contact with the aqueous subphase, and the last slab is in contact with vapor.

Parameter	LysoPC	PA inverted bilayer	PA trilayer
σ (Å)	$3.6^{+0.3}_{-0.5}$	$1.3^{+0.4}$	$1.3^{+0.4}$
d_1(Å)	$6.0^{+4.0}_{-1.0}$	$0.5^{+4.5}_{-0.2}$	$8.0^{+2.0}_{-4.0}$
ρ_1 (e/Å^3)	$0.437^{+0.018}_{-0.038}$	$0.033^{+0.298}_{-0.033}$	$0.387^{+0.028}_{-0.017}$
d_2 (Å)	$8.7^{+0.9}_{-2.2}$	$19.9^{+1.1}_{-2.9}$	$30.9^{+1.8}_{-3.0}$
ρ_2 (e/Å^3)	$0.322^{+0.018}_{-0.047}$	$0.322^{+0.016}_{-0.012}$	$0.285^{+0.052}_{-0.046}$
d_3 (Å)	-	$4.5^{+0.7}_{-0.5}$	$4.4^{+4.0}_{-0.4}$
ρ_3 (e/Å^3)	-	$0.506^{+0.089}_{-0.006}$	$0.458^{+0.142}_{-0.058}$
d_4 (Å)	-	$18.7^{+0.3}_{-0.7}$	$12.8^{+2.5}_{-3.2}$
ρ_4 (e/Å^3)	-	$0.305^{+0.003}_{-0.013}$	$0.121^{+0.091}_{-0.047}$
χ^2	12.8	17.5	

The electron density of the aqueous phase was 0.334 e/Å^3 for both Ca and Ca-free buffers. The error bar for each parameter was calculated based on one standard deviation from the best fit value. Parameters in the fitting were constrained to the following ranges: roughness to 1.3-4 Å, alkyl chain tail electron densities to 0-0.34 e/Å^3 with length 0-21 Å , electron density of lysoPC head group region to 0.37-0.6 e/Å^3 and its thickness to 5-10 Å, electron density of PA head group region to 0.37-0.6 e/Å^3 and its thickness to 4-10 Å, electron density of the head group region of the PA inverted bilayer together with Ca^{2+} to 0.37-0.6 e/Å^3 and its thickness to 4-10 Å.

illustrated in **Figures 1B-1D**. The presence of Ca^{2+} in the subphase had limited effects on the interfacial structure of DPPC molecules, as indicated by both X-ray reflectivity and GIXD measurements (**Figure s2** in **SI**). However, the absence or presence of Ca^{2+} had a substantial effect on the behavior of sPLA$_2$, leading to, respectively, either adsorption of sPLA$_2$ onto the monolayer or to degradation of it.

After sPLA$_2$ was added to the subphase, the surface pressure of the lipid films decreased from 25 mN/m to about 17 mN/m on the Ca-free buffer and to about 10 mN/m on the Ca buffer (**Figure s3A** and **Figure s3B** in **SI**). The surface pressure decreasing with sPLA$_2$ adsorption may have been due to the DPPC film relaxed during the experimental periods. With sPLA$_2$ adsorption, Bragg peaks (**Figure 1B**) of the DPPC monolayer shifted toward a higher Q_{xy} (the out-plane peak shifted from 1.336 to 1.361 Å^{-1} and the in-plane peak from 1.459 to 1.471Å^{-1}), indicating tighter packing with decreased molecular distance and mean molecular area (from 48.4±0.4 to 46.8±0.4 Å^2). The peak positions of the GIXD rods (**Figure 1C**) are similar, with a slight shift toward a lower Q_z (from 0.708 to 0.693 Å^{-1}), indicating a slight decrease of the tilted angles (from 32.2±0.3 to 31.2±0.5°). Therefore, although the surface pressure decreased from 25 mN/m to about 17 mN/m when sPLA$_2$ was adsorbed on the DPPC monolayer, GIXD results showed that DPPC molecules in the gel phase packed more tightly with less tilt, which was consistent with a previous study.[36] Furthermore, in comparing the electron density profiles of the DPPC and DPPC-sPLA$_2$ films (the inset of **Figure 1A**), the total thickness of the monolayer was similar, but the electron densities of the DPPC head group and tail regions in the DPPC-sPLA$_2$ films decreased slightly. As a result of low enzyme concentration and an average sPLA$_2$ electron density similar to the aqueous subphase, it was difficult to identify the position and configuration of sPLA$_2$. However, when lipid parameters remained similar in the single-phase box model, adding an extra layer below the DPPC head group region significantly improved the quality of fits to the data (**Table 1**). This additional layer attributed to the adsorption of sPLA$_2$ to the monolayer.[36, 37] Further increasing model complexity with composition-space refinement may provide more details about protein-lipid interactions,[38-40] which is beyond the scope of this study and will be investigated systematically in future.

The reflectivity curve of the degraded DPPC film (**Figure 1A)** exhibited secondary peaks and less pronounced decay of peak intensities, indicating domain and secondary structure formation. It was difficult to achieve satisfactory fitting to these data using the single-phase box model, but an incoherent multi-phase box model provided a reasonable fitting (green line in **Figure 1A**). In addition, after DPPC degradation, the two GIXD peaks of DPPC were replaced by five strong and sharp GIXD peaks (**Figure 1D**), indicating the formation of new highly ordered crystal structures whose coherence length was close to the limit of the X-ray measurements.

2. PA and lysoPC films on Ca buffer

2.1 Molecular packing structures across interface.

To determine the film structure at the interface after DPPC degradation, the molecular packing of the two degradation products, PA and lysoPC, and their equimolar mixture (PA-lysoPC) on Ca buffer was investigated. The X-ray measurements on the lysoPC film were conducted at a surface pressure of 10 mN/m, which was close to the

quasi-equilibrium surface pressure of the degraded DPPC film. The X-ray reflectivity data of the lysoPC film (**Figure 2A**) was fitted using a single-phase two-box model (structural parameters are listed in **Table 2**) to yield an electron density profile (**Figure 2B**) of a monolayer.

The normalized reflectivity R/R_F of PA on the Ca buffer exhibited no decay along the Q_z direction (**Figure 2A**). The dip just above the critical angle (Q_{xy}=0.0217 Å^{-1}) indicated that the film electron density adjacent to the aqueous phase had an electron density lower than that of the aqueous solution and suggested an inverted bilayer structure.[41,42] However, in this case, a single-phase inverted bilayer model was inadequate to provide a good fit for the X-ray reflectivity data of the PA film, as shown by the blue dashed line in the top plot of **Figure 2A**. A reasonable fit (the red solid line in the top plot of **Figure 2A**) was obtained using a multi-phase box model containing an inverted bilayer and a trilayer, which was similar to the model used to analyze a collapsed arachidic acid film on a Ca buffer.[42]

The best fit obtained using the two-phase model for the PA film at a constant pressure of 2 mN/m showed that the inverted bilayer structure of PA covered most (89^{+6}_{-11}%) of the interface; corresponding structural parameters are listed in **Table 2**. The tail length of both leaflets was approximately equal to the length of the fully extended PA alkyl chain, 20.3 Å.[43] The head group region displayed a high electron density of 0.506 e/Å^3 due to the strong electrostatic interaction of Ca^{2+} with the carboxyl group (COO^-) of PA, which overcame the entropy decrease and hydrophobic effects of the tails and stabilized the inverted bilayer structure.[42] The fit suggest that a very thin, low density layer exists between the lipid bilayers and the aqueous phase, similar to a deficit layer (a region where electron density is close to 0) structure observed for n-hexatriacontane (n-$C_{36}H_{74}$) monolayers deposited on pure water,[44] though the thickness of this structure of 0.5 Å is below the spatial resolution of these measurements. Coexisting with the interfacial bilayer phase was a trilayer; corresponding structural parameters are listed in **Table 2**. The fitting errors for the trilayers were relatively large because of their small surface coverage.

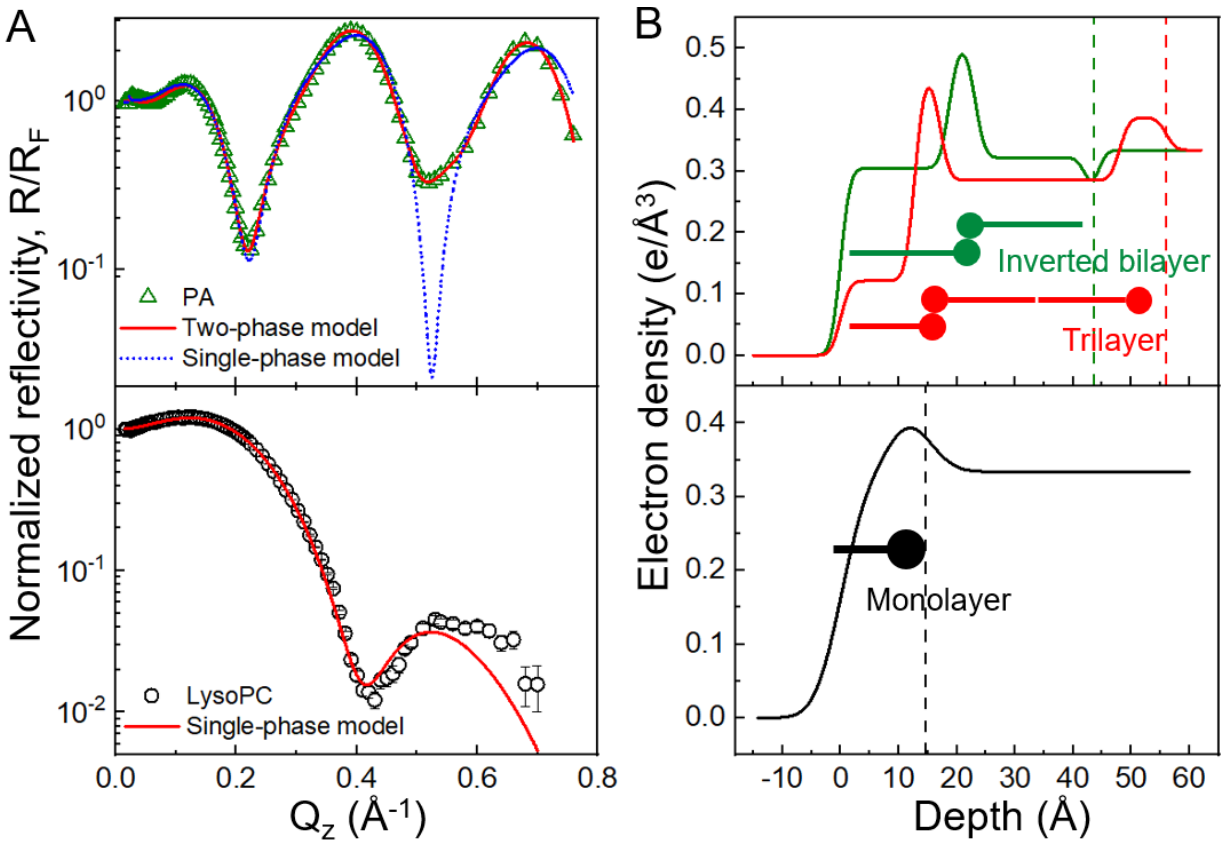

Figure 2. X-ray reflectivity and electron density profiles of PA and lysoPC on Ca buffer at constant pressure: 2 mN/m for PA and 10 mN/m for lysoPC. (A) Normalized X-ray reflectivity of PA (green triangles) and lysoPC (black circles) on Ca buffer. In the top plot, the blue dashed line represents the fit from applying a single-phase inverted bilayer model, and the red solid line represents the fit from applying a multi-phase box model consisting of an inverted bilayer phase and a trilayer phase. The red line in the bottom plot represents the fit from applying a single-phase two-box model. The structural parameters corresponding to the red solid lines are listed in **Table 2.** (B) Electron density profiles of PA (red line for trilayer and green line for inverted bilayer in the top plot) and lysoPC (black line in bottom plot) resulted from the best model fitting (red solid lines) in (A). The dashed lines with the same color indicate the position of water surface in the corresponding electron density profiles. The surface coverages of the inverted bilayer and trilayer in the PA film were 89% and 11%, respectively. The schematic molecular structures represent lipid packing structures (consistent color theme as the electron density profiles).

X-ray reflectivity and GIXD measurements were conducted on PA films at two constant pressures, 2 and 10 mN/m. At both pressures, the film collapsed with time and the average molecular surface area decreased with time. At 10 mN/m, the collapse rate was greater and high intensity diffraction peaks were observed in the high Q_z region which interfered with the reflectivity peaks (**Figure s4** in **SI**). This probably indicated the formation of an interfacial component with more layers at the interface.

2.2 Molecular packing structures parallel to interface.

Five strong and sharp GIXD peaks were observed for the PA film at 2 mN/m (**Figure 3A**). The positions and widths of the Bragg peaks and Bragg rods of PA film on the Ca buffer were similar to those of the degraded DPPC film on the Ca buffer, which suggested that the interfacial lateral packing structures of the PA-Ca^{2+} complex formed for pure PA on the Ca buffer were similar to those established in PA domains after DPPC degradation on the Ca buffer. The peak intensities of the former were higher than those of the latter because the surface coverage of the PA domains was reduced in the degraded DPPC film. In addition, these GIXD peaks were not observed on the PA films on Ca-free buffer at the same surface pressure of 2 mN/m or at 10 mN/m (**Figure s5** in **SI**). The lysoPC film exhibited no GIXD peaks on the Ca buffer (**Figure 3B**), indicating a disordered molecular packing of the lysoPC monolayer at the interface.

The five GIXD peaks of the PA film on the Ca buffer and of the degraded DPPC films were scattered from the highly ordered PA-Ca^{2+} complex. Specifically, the Bragg rod intensity of the first peak at Q_{xy} = 1.075 $Å^{-1}$ showed no decay throughout the entire Q_z range (0-0.6 $Å^{-1}$) (**Figure 3A**), indicating that this peak was from an ordered Ca^{2+} layer. Weak second-order peaks from the ordered Ca^{2+} layer were recorded at Q_{xy} = 2.15 $Å^{-1}$ for both PA and degraded DPPC films, with a Bragg rod intensity variation in Q_z similar to those of the 1.075 $Å^{-1}$ peaks (**Figure s6** in **SI**). The peaks appearing in the other Bragg rods have widths $\Delta Q_z \leq 0.5$ $Å^{-1}$, indicating a layer thicker than 12 Å (obtained from $2\pi/\Delta Q_z$) that we attribute to alkyl chain ordering. It is

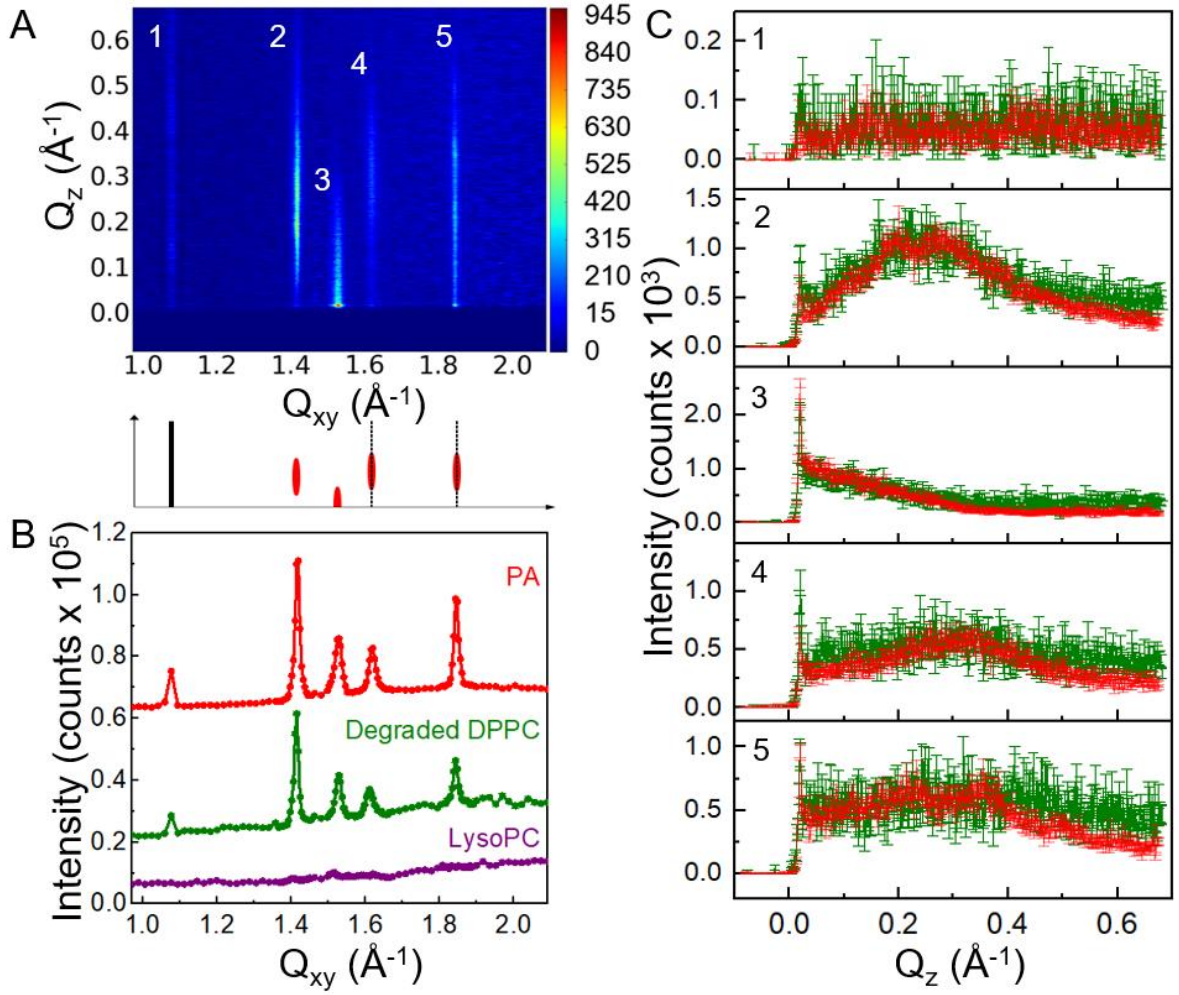

Figure 3. GIXD for PA and lysoPC on Ca buffer at constant pressures: 2 mN/m for PA and 10 mN/m for lysoPC. (A) Two-dimensional GIXD result of PA with schematic plot to classify peaks scattered from Ca^{2+} layer (black lines) or alkyl chains of PA (red ellipses). (B) Bragg peaks of PA (red), degraded DPPC (green), and lysoPC (purple) films on Ca buffer. The data are offset and the solid lines connecting the dots are provided for clarity. (C) Bragg rods of degraded DPPC (green) and PA (red) films on Ca buffer. The intensity from PA is reduced by half for comparison to the degraded DPPC. The five plots from top to bottom correspond respectively to the low to high Q_{xy} features labelled in (A).

possible that two other first-order Ca^{2+} peaks may have overlapped the Bragg peaks of the alkyl chains at 1.62 $Å^{-1}$ and 1.84 $Å^{-1}$; thus, the three peaks implied an oblique unit cell of the organized Ca^{2+} with parameters of a = 3.9±0.1 Å, b = 6.7±0.1 Å, angle γ = 60.5±0.5°, and area = 22.8±0.1$Å^2$. The highly organized Ca^{2+} layer suggested formation of fatty acid-divalent metal ion superstructures.

The three Bragg peaks with Q_{xy} at 1.42 $Å^{-1}$, 1.53 $Å^{-1}$, and 1.62 $Å^{-1}$ may have been scattered from the same organization of PA alkyl chains that exhibited oblique packing structures, as the peak positions of their Bragg rods roughly satisfied the relationship of $Q_{z3} = Q_{z1}+Q_{z2}$,[45] with Q_{z1} (0.25±0.02 $Å^{-1}$), Q_{z2} (0 $Å^{-1}$), and Q_{z3} (0.27±0.04 $Å^{-1}$). As a result, the oblique unit cell parameters of alkyl chains were a = 4.8±0.1 Å, b = 5.1±0.1 Å, angle γ = 53.5±0.3°, and area = 19.8±0.1 $Å^2$, which are consistent with a previously reported area (19.7 $Å^2$) for the tightest packed alkyl chain of PA on the Ca buffer.[46] The widths of the Bragg rod peaks (ΔQ_z) were about 0.4 $Å^{-1}$ for these three peaks (the 2nd, 3rd, and 4th frames **in Figure 3C**), which indicated a single tail thickness and suggested that the leaflets of the PA multilayers were incoherent so each leaflet monolayer scattered as an individual monolayer rather than as one coupled entity.[43, 47] It was difficult to achieve accurate fitting for the Bragg rod peak at 1.84 $Å^{-1}$ (the 5th plot of **Figure 3C**), because of the low signal to noise ratio. The molecular organization corresponding to this peak requires further investigation in the future.

A separate study by Zhai et al.[15] on the degradation of DPPC film suggested that the Bragg peak at 1.53 $Å^{-1}$ was from a hexagonal packing structure of the PA alkyl chain, and the Bragg peak at 1.42 $Å^{-1}$ was assumed from an additional phase whose structure was uncertain. However, that study reported only two GIXD Bragg peaks in the range from 1.3 to 1.6 $Å^{-1}$ without considering the peak at 1.62 $Å^{-1}$. In summary, GIXD results obtained from PA films or degraded DPPC films are difficult to interpret; however, quantitative analysis suggests the presence of an oblique packing structure of PA-Ca^{2+} complexes at the interface.

3. Molecular packing structures of PA-lysoPC film and degraded DPPC film.

To better identify the film structure after DPPC degradation, X-ray reflectivity measurements were conducted on a film formed by an equimolar mixture of PA and lysoPC on the Ca buffer at a constant pressure of 10 mN/m. This pressure was close to the quasi-equilibrium surface pressure of the degraded DPPC film. The normalized X-ray reflectivity data of PA-lysoPC and degraded DPPC are shown in **Figure 4A**, which present additional peaks comparing to DPPC monolayers. The best fit for both films was achieved by employing the model including a combination of trilayer and inverted bilayer PA domains and monolayer lysoPC domains. The electron density profiles are presented in **Figure 4B**, and structural parameters are listed in **Table 3**. The two-phase box model with monolayer lysoPC domains and inverted bilayer PA domains were

Table 3. Structural parameters resulted from model fitting of the X-ray reflectivity data of PA-lysoPC and degraded DPPC films on a Ca buffer by applying a three-phase box model (corresponding to the green solid lines in **Figure 4A**). The first slab (labelled 1) is in contact with the aqueous subphase, and the last slab is in contact with vapor.

Lipid films	PA-lysoPC			Degraded DPPC		
Parameter	LysoPC monolayer	PA inverted bilayer	PA trilayer	LysoPC monolayer	PA inverted bilayer	PA trilayer
ω	$0.81^{+0.09}_{-0.24}$	$0.10^{+0.30}_{-0.06}$	$0.09^{+0.13}_{-0.08}$	$0.78^{+0.06}_{-0.29}$	$0.13^{+0.36}_{-0.11}$	$0.09^{+0.31}_{-0.07}$
σ (Å)	$3.7^{+0.3}_{-0.6}$	$1.4^{+0.1}_{-0.1}$	$1.4^{+0.1}_{-0.1}$	$3.7^{+0.4}_{-1.2}$	$1.7^{+0.1}_{-0.4}$	$1.7^{+0.1}_{-0.4}$
d_1 (Å)	$6.1^{+3.9}_{-1.1}$	$1.1^{+3.9}_{-0.6}$	$7.8^{+1.6}_{-3.5}$	$5.7^{+4.3}_{-0.7}$	$1.9^{+3.2}_{-1.6}$	$7.2^{+2.8}_{-3.2}$
ρ_1 (e/Å³)	$0.487^{+0.113}_{-0.097}$	$0.012^{+0.268}_{-0.012}$	$0.382^{+0.218}_{-0.012}$	$0.482^{+0.118}_{-0.108}$	$0.175^{+0.142}_{-0.175}$	$0.432^{+0.068}_{-0.062}$
d_2 (Å)	$9.4^{+1.4}_{-3.2}$	$20.0^{+0.8}_{-2.8}$	$27.5^{+2.5}_{-2.0}$	$9.2^{+1.7}_{-3.7}$	$20.3^{+0.7}_{-4.5}$	$28.1^{+2.0}_{-2.4}$
ρ_2 (e/Å³)	$0.306^{+0.034}_{-0.156}$	$0.328^{+0.012}_{-0.147}$	$0.299^{+0.035}_{-0.191}$	$0.301^{+0.039}_{-0.190}$	$0.303^{+0.037}_{-0.233}$	$0.319^{+0.021}_{-0.190}$
d_3 (Å)		$4.1^{+2.3}_{-0.1}$	$4.2^{+5.8}_{-0.2}$		$4.1^{+5.9}_{-0.1}$	$4.0^{+6.0}$
ρ_3 (e/Å³)		$0.509^{+0.091}_{-0.139}$	$0.539^{+0.061}_{-0.169}$		$0.563^{+0.037}_{-0.163}$	$0.557^{+0.043}_{-0.157}$
d_4 (Å)		$19.2^{+0.4}_{-2.4}$	$19.0^{+0.7}_{-0.7}$		$18.8^{+0.6}_{-4.5}$	$18.7^{+0.3}_{-1.2}$
ρ_4 (e/Å³)		$0.236^{+0.104}_{-0.105}$	$0.235^{+0.086}_{-0.108}$		$0.267^{+0.073}_{-0.125}$	$0.179^{+0.055}_{-0.087}$
χ^2	2.3			5.4		

The electron density of the aqueous phase was 0.334 e/Å³. The error bar for each parameter was calculated based on one standard deviation from the best fit value. The parameter ω is the fractional coverage of each interfacial phase. Parameters in the fitting were constrained to the following ranges: roughness to 1.3-4 Å, electron density of alkyl chains to 0-0.34 e/Å³ and thickness to 0-21 Å, electron density of the PA head group region to 0.37-0.6 e/Å³ and thickness to 4-10 Å, the electron density of the head group region of the PA inverted bilayer together with Ca^{2+} to 0.37-0.6 e/Å³ and thickness to 4-10 Å, thickness of lysoPC head group region to 5-10 Å and electron density to 0.37-0.6 e/Å³, thickness of the deficit layer to 0-5 Å.

inadequate to provide a good fit to the data, as shown by the blue dashed lines in **Figure 4A**. In addition, the domain distribution of the PA-lysoPC film on the Ca buffer obtained using the fluorescence microscopy suggested that multi-phases co-existed at the interface and that most of the interface was covered by the lysoPC liquid phase (**Figure s7** in **SI**); these results were consistent with the X-ray data for the PA-lysoPC film. Comparison of the X-ray reflectivity and GIXD data for DPPC films degraded by $sPLA_2$ and films consisting of equimolar mixtures of PA and lysoPC indicated similar packing structures. Our analysis suggests that these interfaces are covered mostly by monolayer lysoPC with the rest of the interface covered by a complex organization of inverted bilayer and possibly trilayer structures of PA (**Figure 4C**). In the figure, the position and configuration of $sPLA_2$ after film degradation were speculated based on literature. [8, 9, 11, 17, 18, 37, 48]

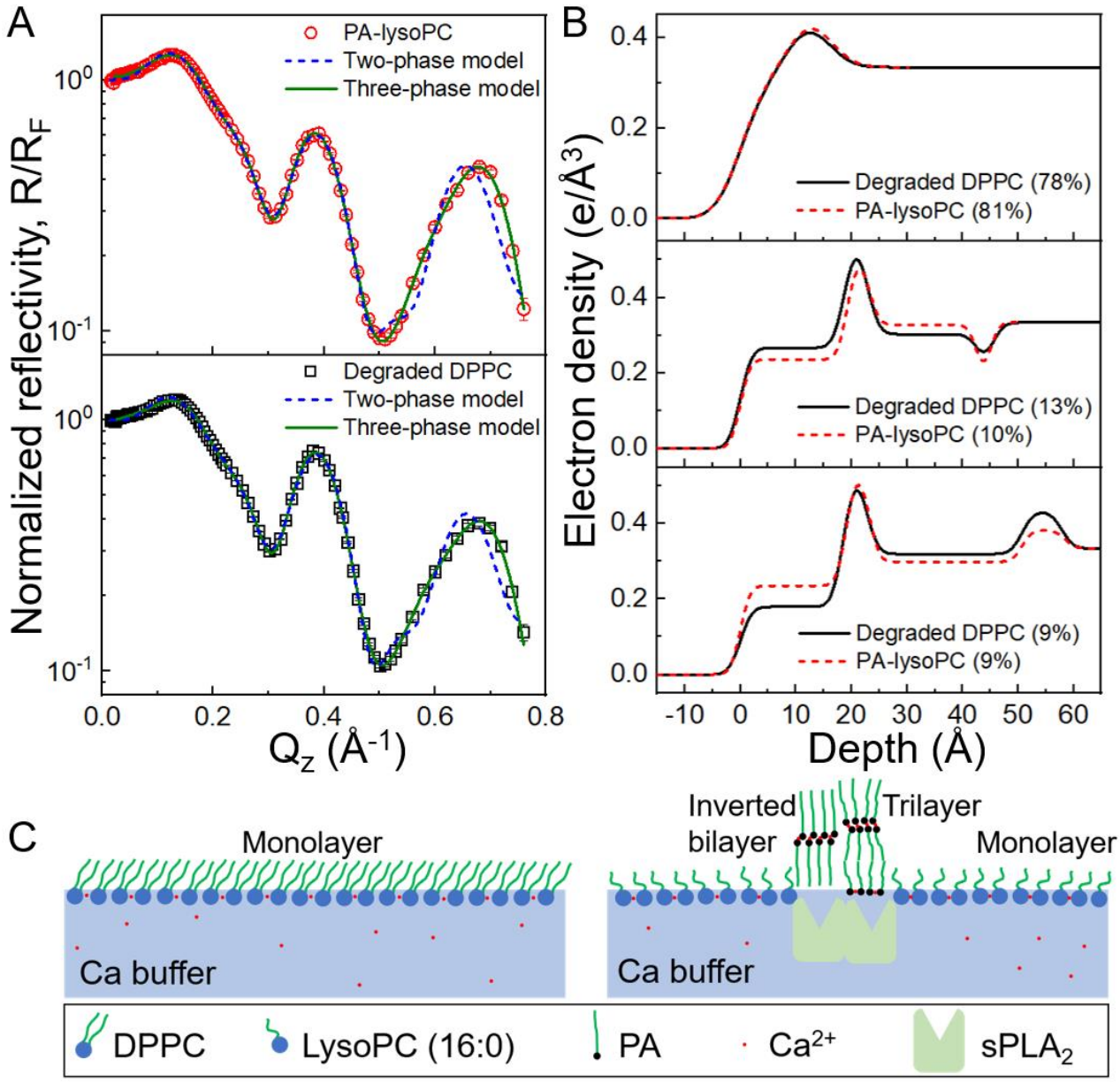

Figure 4. Interfacial organization of mixed PA-lysoPC films and degraded DPPC films on Ca buffer. (A) Normalized reflectivity of mixed 1:1 PA-lysoPC (red circles) and degraded DPPC (black squares) films on Ca buffer. The blue dashed lines in both plots represent the fitting resulted from a two-phase box model consisting of inverted PA bilayer domains and lysoPC monolayer domains. The green dashed lines in both plots represent the fitting resulted from a three-phase box model consisting of a trilayer phase, an inverted bilayer phase, and a monolyer phase. The resulted structural parameters are listed in **Table 3**. (B) Electron density profiles of the monolayer, bilayer, and trilayer phases calculated from the model fitting using the three-phase box models (green solid lines in **Figure 4A**). The percentages in the parenthese represent the surface coverage of each domain structure in the corresponding film. (C) Schematic plot of molecular packing structures of DPPC (left) and degraded DPPC (right) films on Ca buffer at the gas-liquid interface.

4. Discussion

Upon DPPC degradation by $sPLA_2$ on a Ca buffer, one of the degradation products, PA, formed a complex with Ca^{2+} and generated highly ordered structures at the interface. Complex formation was most likely due to strong electrostatic interactions between Ca^{2+} and deprotonated carboxyl groups of PA molecules. Although PA-Ca^{2+} complex formation after DPPC degradation was previously observed by other techniques such as fluorescence microscopy,[17, 48] polarization-modulated Fourier transform infrared spectroscopy,[14] sum frequency spectroscopy,[49] and surface-viscosity measurement,[50] to our knowledge, this study is the first to reveal the molecular packing structures of degraded DPPC films.

Formation of highly-ordered multilayers of PA-Ca^{2+} complexes provides a molecular-level explanation for PA-induced liposome permeation. When water was used as the subphase, incorporation of PA into DPPC monolayers was reported to increase the conformational ordering rather than destabilizing the monolayer structure of DPPC[51] and only slightly increased permeation of DPPC liposomes.[52] However, at the same temperature (25 °C) in a non-acid buffer (pH $\geqslant$ 7) with Ca^{2+}, significant instant release of drugs from liposomes was observed when adding a sufficient amount of PA.[53] A comprehensive explanation relies on the formation of distinct PA packing structures in different buffers. When highly ordered multilayers of PA-Ca^{2+} complexes were generated with sufficient Ca^{2+} in alkaline environment,[54] the surface coverage of liposomes was reduced, generating holes on the surface and leading to burst drug release. However, in water without Ca^{2+}, the disturbance of PA on phospholipid membranes was much weaker.

The other DPPC degradation product, lysoPC, has also been reported to induce permeation of liposomes and cell membranes, showing less dependence on the presence of Ca^{2+} in buffer conditions.[22, 55] This is due to a different mechanism from the PA-induced liposome permeation. Adding lysoPC to DPPC liposomes reduced surface rigidity and led to membrane permeation.

$sPLA_2$ catalyzed degradation redistributed lipid degradation products into the third dimension, producing multilayer PA domains that co-exist with loosely packed lysoPC domains, thereby damaging the structural integrity of the original lipid layer. This mechanism of degradation provides an explanation for the bursting of liposomes after a latency period of mixing liposomes with $sPLA_2$. $sPLA_2$ catalyzed degradation and liposome permeation of other long-chain saturated phospholipids (such as distearoylphosphatidylcholine) were also reported to exhibit a strong dependence on Ca^{2+}.[53] A similar mechanism may be relevant in this case as well, in which $sPLA_2$ catalyzed degradation produces heterogeneities that destabilize the membrane.

Conclusions

By integrating a Langmuir trough with X-ray reflectivity and GIXD interface-sensitive techniques, molecular-level insights were gained into the interaction of $sPLA_2$ with DPPC. On Ca-free buffer, $sPLA_2$ was absorbed to the DPPC monolayer, resulting in a more tightly packed monolayer with less tilt. With Ca^{2+} in the buffer, $sPLA_2$ catalyzed degradation of DPPC and disrupted the ordered monolayer. Multiple phases were generated at the interface by the degradation products. One of the DPPC degradation products, PA, formed complexes with Ca^{2+} that displayed highly-ordered multi-layer structures. The other degradation product, lysoPC, exists as a fluid monolayer at the interface. The distinct packing structures of PA and lysoPC phases formed after DPPC degradation provide a molecular-level explanation for PA and lysoPC induced liposome permeation. This study utilized DPPC and $sPLA_2$ from bee venom as a model phospholipid and a model enzyme, but the phenomena and the underlying mechanism may be extended to a category of similar phospholipids and phospholipases. The results of this study advance our understanding on the role of $sPLA_2$ in related physiological processes and lead to a mechanism-based approach to designing and optimizing lipid-based nanomedicines.

Conflicts of interest

There are no conflicts to declare.

Acknowledgements

The study is supported by the NSF Nanomanufacturing Program (NSF CAREER #1350731). ChemMatCARS Sector 15 is principally supported by the Divisions of Chemistry (CHE) and Materials Research (DMR), National Science Foundation, under grant number NSF/CHE-1834750. Use of the Advanced Photon Source, an Office of Science User Facility operated for the U.S. Department of Energy (DOE) Office of Science by Argonne National Laboratory, was supported by the U.S. DOE under Contract No. DE-AC02-06CH11357. The authors are grateful to Professor Ursula Perez-Salas for access to her laboratory and for much helpful advice. The authors thank Professor Ka Yee Lee research group at the University of Chicago for providing the design of the trough.

Notes and references

1. D. Bobo, K. J. Robinson, J. Islam, K. J. Thurecht and S. R. Corrie, *Pharmaceutical Research*, 2016, **33**, 2373-2387.
2. A. H. Hansen, O. G. Mouritsen and A. Arouri, *International Journal of Pharmaceutics*, 2015, **491**, 49-57.
3. D. Y. Hui, *Current opinion in lipidology*, 2012, **23**, 235-240.
4. N. R. Webb, *Current Opinion in Lipidology*, 2005, **16**, 341-344.
5. T. Abe, K. Sakamoto, H. Kamohara, Y. i. Hirano, N. Kuwahara and M. Ogawa, *International Journal of Cancer*, 1997, **74**, 245-250.
6. S. I. Yamashita, J. I. Yamashita and M. Ogawa, *British Journal Of Cancer*, 1994, **69**, 1166.
7. T. Honger, K. Jorgensen, R. L. Biltonen and O. G. Mouritsen, *Biochemistry*, 1996, **35**, 9003-9006.
8. D. L. Scott, Z. Otwinowski, M. H. Gelb and P. B. Sigler, *Science*, 1990, **250**, 1563-1566.
9. D. L. Scott, S. P. White, Z. Otwinowski, W. Yuan, M. H. Gelb and P. B. Sigler, *Science (New York, NY)*, 1990, **250**, 1541.
10. M. Gudmand, S. Rocha, N. S. Hatzakis, K. Peneva, K. Müllen, D. Stamou, H. Uji-I, J. Hofkens, T. Bjørnholm and T. Heimburg, *Biophysical Journal*, **98**, 1873-1882.

11. A. Reichert, H. Ringsdorf and A. Wagenknecht, *Biochimica et Biophysica Acta (BBA)-Biomembranes*, 1992, **1106**, 178-188.
12. K. Balashev, V. Atanasov, M. Mitewa, S. Petrova and T. Bjørnholm, *Biochimica et Biophysica Acta (BBA) - Biomembranes*, 2011, **1808**, 191-198.
13. K. Balashev, N. John DiNardo, T. H. Callisen, A. Svendsen and T. Bjørnholm, *Biochimica et Biophysica Acta (BBA) - Biomembranes*, 2007, **1768**, 90-99.
14. M. Grandbois, B. Desbat and C. Salesse, *Biophysical Chemistry*, 2000, **88**, 127-135.
15. X. Zhai, J. Li, G. Brezesinski, Q. He, H. Möhwald, L. Lai, Y. Liu, L. Liu and Y. Gao, *ChemBioChem*, 2003, **4**, 299-305.
16. D. Grainger, A. Reichert, H. Ringsdorf and C. Salesse, *Febs Letters*, 1989, **252**, 73-82.
17. J. Li, Z. Chen, X. Wang, G. Brezesinski and H. Möhwald, *Angewandte Chemie International Edition*, 2000, **39**, 3059-3062.
18. K. M. Maloney and D. W. Grainger, *Chemistry and Physics of Lipids*, 1993, **65**, 31-42.
19. C. Y. Hong, C.-T. Han and L. Chao, *Langmuir*, 2016, **32**, 6991-6999.
20. W. R. Burack, Q. Yuan and R. L. Biltonen, *Biochemistry*, 1993, **32**, 583-589.
21. W. R. Burack, A. R. Dibble, M. M. Allietta and R. L. Biltonen, *Biochemistry*, 1997, **36**, 10551-10557.
22. A. Arouri and O. G. Mouritsen, *Progress in Lipid Research*, 2013, **52**, 130-140.
23. K. N. Belosludtsev, N. V. Belosludtseva, A. V. Agafonov, M. E. Astashev, A. S. Kazakov, N.-E. L. Saris and G. D. Mironova, *Biochimica et Biophysica Acta (BBA) - Biomembranes*, 2014, **1838**, 2600-2606.
24. H. Pourhassan, G. Clergeaud, A. E. Hansen, R. G. Østrem, F. P. Fliedner, F. Melander, O. L. Nielsen, C. K. O'Sullivan, A. Kjær and T. L. Andresen, *Journal of Controlled Release*, 2017, **261**, 163-173.
25. M. Murakami and I. Kudo, *Current opinion in lipidology*, 2003, **14**, 431-436.
26. J. D. Bell, M. Burnside, J. A. Owen, M. L. Royall and M. L. Baker, *Biochemistry*, 1996, **35**, 4945-4955.
27. E. D. Bent and J. D. Bell, *Biochimica et Biophysica Acta (BBA) - Lipids and Lipid Metabolism*, 1995, **1254**, 349-360.
28. W. Bu and M. L. Schlossman, *Synchrotron Light Sources and Free-Electron Lasers: Accelerator Physics, Instrumentation and Science Applications*, 2014, 1-33.
29. K. Kjaer, J. Als-Nielsen, C. A. Helm, L. A. Laxhuber and H. Möhwald, *Physical Review Letters*, 1987, **58**, 2224-2227.
30. P. S. Pershan and M. Schlossman, *Liquid Surfaces and Interfaces: Synchrotron X-ray Methods*, Cambridge University Press, 2012.
31. L. G. Parratt, *Physical review*, 1954, **95**, 359.
32. A. M. Tikhonov, S. V. Pingali and M. L. Schlossman, *The Journal of chemical physics*, 2004, **120**, 11822-11838.
33. P. Dutta, J. B. Peng, B. Lin, J. B. Ketterson, M. Prakash, P. Georgopoulos and S. Ehrlich, *Physical Review Letters*, 1987, **58**, 2228-2231.
34. J. Als-Nielsen, F. Christensen and P. S. Pershan, *Physical Review Letters*, 1982, **48**, 1107-1110.
35. W. Bu and D. Vaknin, *Langmuir*, 2008, **24**, 441-447.
36. U. Dahmen-Levison, G. Brezesinski and H. Möhwald, *Thin Solid Films*, 1998, **327**, 616-620.
37. W.-N. Huang, Y.-H. Chen, C.-L. Chen and W. Wu, *Langmuir*, 2011, **27**, 7034-7041.
38. P. Shekhar, H. Nanda, M. Lösche and F. Heinrich, *Journal of applied physics*, 2011, **110**, 102216-10221612.
39. M. Schalke, P. Krüger, M. Weygand and M. Lösche, *Biochimica et Biophysica Acta (BBA) - Biomembranes*, 2000, **1464**, 113-126.
40. H. P. Vacklin, F. Tiberg, G. Fragneto and R. K. Thomas, *Langmuir*, 2005, **21**, 2827-2837.
41. W. Bu, H. Yu, G. Luo, M. K. Bera, B. Hou, A. W. Schuman, B. Lin, M. Meron, I. Kuzmenko, M. R. Antonio, L. Soderholm and M. L. Schlossman, *The Journal of Physical Chemistry B*, 2014, **118**, 10662-10674.
42. D. Vaknin, W. Bu, S. K. Satija and A. Travesset, *Langmuir*, 2007, **23**, 1888-1897.
43. W. J. Sun, R. M. Suter, M. A. Knewtson, C. R. Worthington, S. Tristram-Nagle, R. Zhang and J. F. Nagle, *Physical Review E*, 1994, **49**, 4665-4676.
44. T. R. Jensen, M. Østergaard Jensen, N. Reitzel, K. Balashev, G. H. Peters, K. Kjaer and T. Bjørnholm, *Physical Review Letters*, 2003, **90**, 086101.
45. V. M. Kaganer, H. Möhwald and P. Dutta, *Reviews of Modern Physics*, 1999, **71**, 779-819.
46. D. K. Schwartz, R. Viswanathan and J. A. Zasadzinski, *The Journal of Chemical Physics*, 1994, **101**, 7161-7168.
47. C. E. Miller, J. Majewski, E. B. Watkins, D. J. Mulder, T. Gog and T. L. Kuhl, *Physical Review Letters*, 2008, **100**, 058103.
48. D. W. Grainger, A. Reichert, H. Ringsdorf and C. Salesse, *Biochimica et Biophysica Acta (BBA)-Biomembranes*, 1990, **1023**, 365-379.
49. C. Y. Tang, Z. Huang and H. C. Allen, *The Journal of Physical Chemistry B*, 2011, **115**, 34-40.
50. D. W. Deamer and D. G. Cornwell, *Biochimica et Biophysica Acta (BBA) - Lipids and Lipid Metabolism*, 1966, **116**, 555-562.
51. G. Ma and H. C. Allen, *Langmuir*, 2007, **23**, 589-597.
52. H. Jespersen, J. H. Andersen, H. J. Ditzel and O. G. Mouritsen, *Biochimie*, 2012, **94**, 2-10.
53. A. Agafonov, E. Gritsenko, K. Belosludtsev, A. Kovalev, O. Gateau-Roesch, N.-E. L. Saris and G. D. Mironova, *Biochimica et Biophysica Acta (BBA) - Biomembranes*, 2003, **1609**, 153-160.
54. V. Dupres, S. Cantin, F. Benhabib, F. Perrot, P. Fontaine, M. Goldmann, J. Daillant and O. Konovalov, *Langmuir*, 2003, **19**, 10808-10815.
55. C. J. A. Van Echteld, B. De Kruijff, J. G. Mandersloot and J. De Gier, *Biochimica et Biophysica Acta (BBA) - Biomembranes*, 1981, **649**, 211-220.

Degradation of DPPC catalyzed by $sPLA_2$ resulted in a mixture of highly-ordered multilayer domains and loosely packed monolayer phase

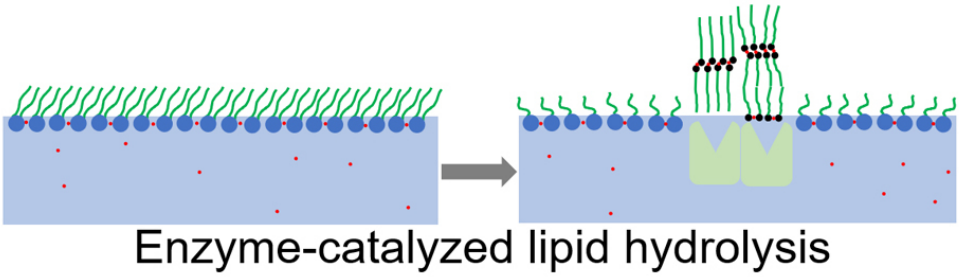

80x24mm (300 x 300 DPI)